

See discussions, stats, and author profiles for this publication at: <https://www.researchgate.net/publication/231647380>

# Processing Core/Alloy/Shell Nanoparticles: Tunable Optical Properties and Evidence for Self-Limiting Alloy Growth

ARTICLE in THE JOURNAL OF PHYSICAL CHEMISTRY C · MAY 2011

Impact Factor: 4.77 · DOI: 10.1021/jp201151m

---

CITATIONS

17

READS

42

---

## 9 AUTHORS, INCLUDING:



Wenjie Wu

University of California, Davis

23 PUBLICATIONS 911 CITATIONS

[SEE PROFILE](#)



Peter Njoki

Hampton University

45 PUBLICATIONS 2,405 CITATIONS

[SEE PROFILE](#)



Hui Zhao

Syracuse University

11 PUBLICATIONS 44 CITATIONS

[SEE PROFILE](#)



Patrick Lutz

Syracuse University

6 PUBLICATIONS 29 CITATIONS

[SEE PROFILE](#)

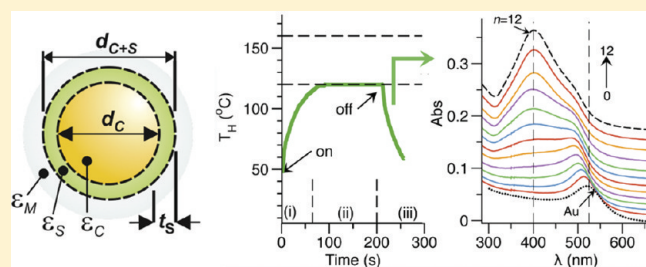
# Processing Core/Alloy/Shell Nanoparticles: Tunable Optical Properties and Evidence for Self-Limiting Alloy Growth

Wenjie Wu,<sup>†,§</sup> Peter N. Njoki,<sup>†,§</sup> Hyunjoo Han,<sup>†</sup> Hui Zhao,<sup>‡</sup> Eric A. Schiff,<sup>‡</sup> Patrick S. Lutz,<sup>†</sup> Louis Solomon,<sup>†</sup> Sean Matthews,<sup>†</sup> and Mathew M. Maye<sup>\*,†</sup>

<sup>†</sup>Department of Chemistry and <sup>‡</sup>Department of Physics, Syracuse University, Syracuse, New York 13244, United States

 Supporting Information

**ABSTRACT:** The postsynthetic processing of nanomaterials may allow researchers to reach specific properties, morphologies, or phase regimes that are not accessible by simple synthesis alone. Here, we take advantage of atomic interdiffusion at nanoparticle interfaces to fabricate core/alloy and core/alloy/shell nanoparticles. Modest temperature changes were found to have profound effects for the interfacial alloying of the confined nanosystem. The alloy formation and subsequent interdiffusion allowed us to tailor nanoparticle composition and ultrastructure, as well as surface plasmon response. This processing step, which involves the layer-by-layer formation of a core/alloy/shell morphology, utilizes hydrothermal annealing provided by automated microwave irradiation to control solute deposition, as well as alloy thickness. As a proof-of-principle system, we employed a Au/Au<sub>x</sub>Ag<sub>1-x</sub>/Ag nanosystem, due, in large part, to its miscible phase diagram and rich plasmonic behavior. Nanostructure morphology was characterized by TEM and STEM, and compositional analysis was performed via selective area EDX and XPS. The resulting surface plasmon resonance signatures were modeled as a function of alloy or monometallic shell thickness, as well as alloy composition, using the discrete dipole approximation method. A proposed shell growth mechanism is described, which involves the competition between a classical ripening system at low temperature and a self-limiting growth at high temperature, the latter of which may be driven by an alloy order-disorder phenomena at the interface. These optical and growth models strongly correlate with the experimental results, namely, that the plasmon resonance is highly tunable on shell thickness and alloy composition and that alloy thickness and interdiffusion are highly tunable by the thermal processing.



## INTRODUCTION

The synthetic methodology for colloidal nanoparticles, such as for metal nanoparticles (NPs) and semiconductive quantum dots (qdots), is a fascinating synergy of wet-chemical reactions with solid-state processing. Much work has been accomplished since the seminal reports for both materials,<sup>1–5</sup> and the knowledge base for colloidal synthesis of nanomaterials and the remarkable electrical, optical, and catalytic properties has grown considerably.<sup>6,7</sup> Up until only recently, fundamental studies have focused on developing protocols to fabricate particles that are crystalline and possess controlled sizes and shapes with a narrow distribution.<sup>1–7</sup> Future generations of NPs will no doubt evolve from these classical examples, and one emerging trend in the field is the potential to “process” as-synthesized nanomaterials toward specific optical, electronic, catalytic, or morphological needs. A first example of this was the growth of metallic<sup>8,9</sup> or semiconductive<sup>10,11</sup> nanorods from spherical precursor seeds. Similarly, larger metal NPs can be grown, creating highly faceted midnano sizes.<sup>12</sup> Inorganic shells can also be deposited at synthesized cores, such as high-band-gap ZnS at CdSe qdots, to improve photoluminescent quantum yields.<sup>13</sup> Another intriguing example is the growth of metallic shells at silica nanospheres, allowing for surface plasmon

oscillation in the near-infrared.<sup>14,15</sup> Morphology can be further tuned in a number of ways, including photomediated mechanisms, as shown for silver NPs being evolved into controlled geometries, such as nanoprisms.<sup>16</sup> The composition of an NP can also be manipulated. In particular, the use of galvanic reactions at the NP interface has proven to be especially interesting.<sup>17–21</sup> Using sacrificial palladium or silver nanocubes, hollow gold shells or cubic gold cages can be fabricated, the process of which can be followed *in situ* by monitoring the plasmonic behavior.<sup>17–21</sup> Another galvanic development is the ability for researchers to alter optical and catalytic properties via reversible ion-exchange reactions in ionic qdot and qrod superlattices.<sup>22–24</sup> Using Cu<sub>2</sub>S or Ag<sub>2</sub>Se qdots or qrods as templates, researchers have shown that Cd<sup>2+</sup> or Pb<sup>2+</sup> will undergo cationic exchange using galvanic potentials to form CdS and PbS of similar qdot size and morphology.<sup>22–24</sup> In these examples, lattice type, reduction potential, solvent, ligand-to-metal binding energies, defect concentrations, and atomic or defect diffusion rates drive the processing.<sup>25</sup> In

**Received:** February 3, 2011

**Revised:** April 16, 2011

**Published:** May 04, 2011

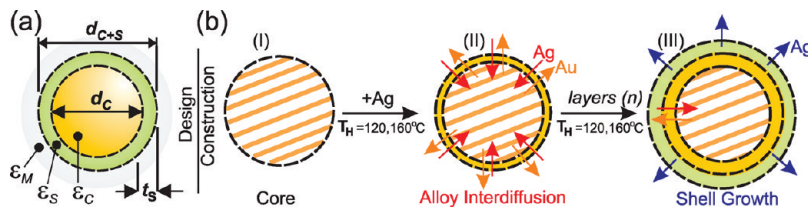


**Figure 1.** (a) A schematic blueprint of the dimensions and factors that govern the Au/Ag SPR response in the present study, namely, core diameter ( $d_c$ ), shell thickness ( $t_s$ ), total NP diameter ( $d_{c+s}$ ), core wavelength-dependent dielectric constant ( $\epsilon_c$ ), shell wavelength-dependent dielectric constant ( $\epsilon_s$ ), and surrounding ligand and media dielectric constant ( $\epsilon_M$ ). (b) An illustration of the processing method. Initial AuNP cores (I) are processed in the presence of  $\text{Ag}^+$  to hydrothermal conditions, which results in the first deposition of  $\text{Ag}^0$ , followed by alloy interdiffusion at the NP interface, resulting in an intermediate alloy shell (II). Further addition of Ag layers ( $n$ ) results in the growth of a Ag shell (III).

addition to chemical reactions at or within the NP core, the thermal processing of NPs is known to improve crystallinity and size distribution using tailored Ostwald ripening.<sup>26–29</sup>

Thus, the processing of presynthesized nanomaterials may allow researchers to reach specific characteristics, morphologies, or phase regimes that are not accessible by simple synthesis alone.<sup>30</sup> While in bulk solids, the diffusion or interdiffusion of impurities, such as dopants, defects, or atoms, over nanoscale distances may not alter properties; similar diffusion, even at modest temperatures, will have profound effects for confined nanosystems.<sup>25</sup> Thus, at the nanoscale, researchers can take advantage of enhanced diffusion rates, high surface free energies, and increased relative defect concentrations.<sup>25,31,32</sup> These effects and the resulting changes to microstructure and lattice type are emerging examples of the Kirkendall effect, which, in addition, to redox potential and atomic and defect diffusion at the NP interface and interior are key.<sup>22–25</sup> It may also be possible to take advantage of atomic diffusion at modest temperatures for nanostructures with nonionic lattices, using the metal-phase behavior of binary or ternary alloys, for example.<sup>33</sup> Such ability may be particularly useful when processing the optical properties of metal NPs.<sup>34–43</sup> However, this ability would require the precise control of the thermal history and reproducibility of the processing step.

In this study, we utilize a novel microwave irradiation (MWI)-based hydrothermal processing method to deposit a Ag shell at Au NP cores (Figure 1). The Au/Ag NP system has been explored previously by researchers using different synthetic strategies, including radiolytic techniques,<sup>38</sup> laser irradiation,<sup>39</sup> galvanic replacement,<sup>17–21,40</sup> coprecipitation,<sup>41</sup> two-phase method,<sup>28</sup> and thermal evolution.<sup>27</sup> Our use of MWI at hydrothermal temperatures ( $T_H$ ) promotes shell growth, as well as core/shell alloying. We recently reported the hydrothermal synthesis of CdSe and CdSe/ZnS qdots.<sup>44</sup> The use of a synthetic reactor for dynamic MWI facilitated automated heating and cooling rates, processing temperature, as well as in situ monitoring of reaction temperature and pressure.<sup>43</sup> By thermally promoting atomic diffusion at the core/shell interface, an alloy intermediate layer is formed, the thickness of which can be tailored by processing temperature and shell thickness. Moreover, the resulting NP plasmonic behavior is highly sensitive to core/shell or core/alloy/shell morphology, which allows for both the precise engineering of the optical properties and the utilization of optical modeling to elucidate the intricacies of particle ultrastructure. To best correlate optical changes to core/shell structure and morphology, we utilized a binary Au/Ag model system, due to strong surface plasmon resonance (SPR) characteristics,<sup>37</sup> as well as a highly miscible binary phase diagram.<sup>33</sup>

## EXPERIMENTAL DETAILS

**Synthesis of Gold Nanoparticle Cores.** Gold nanoparticles ( $\text{Au}, 15.4 \pm 0.7 \text{ nm}$ ) were synthesized by a slightly modified citrate (Cit) reduction procedure.<sup>41</sup> Briefly, an aged 1 mM  $\text{HAuCl}_4$  solution was heated to  $\sim 95^\circ\text{C}$  for 30 min. To this solution was added a warm 38 mM trisodium citrate solution (10 mL) in one aliquot. Upon the initial color change to red, the solution was then immediately cooled to  $\sim 80^\circ\text{C}$  and annealed for 1 h. The sample was then allowed to cool naturally to room temperature and allowed to stir overnight. The solution was then stored protected from light. The Au concentrations were calculated via a measured extinction coefficient of  $2.2 \times 10^8 \text{ L mole}^{-1} \text{ cm}^{-1}$ .

**Layer-by-Layer Shell Growth.** We begin with Au cores synthesized above and deposit shells of Ag in controllable subnanometer layers ( $n$ ). Here, silver ( $\text{AgNO}_3$ ) reduction is achieved using a minimum amount of reducing agent, sodium citrate (Cit), which was found to best reduce the silver ions at the hydrothermal temperatures employed. Moreover, silver ions are added and reduced in a delicate step-by-step (e.g., layer-by-layer) fashion at a ratio ( $r = [\text{Ag}^+]/[\text{Au}]$ ) required to deposit a 0.25–0.50 nm thick shell ( $t_s$ ), based on model calculations for volume change due to shell growth at a constant Au core diameter and NP concentration. For example, in a typical experiment, a 2.2 mL ultrapure water ( $18.2 \text{ M } \Omega$ ) solution of Au ( $[\text{Au}] = 3.6 \text{ nM}$ ,  $d_c = 15.4 \pm 0.7 \text{ nm}$ ), trisodium citrate ( $[\text{Cit}] = 1.36 \text{ mM}$ ), and  $\text{AgNO}_3$  ( $[\text{AgNO}_3] = 0.045 \text{ mM}$ ) is hermetically sealed in 10 mL glass microwave reaction vessels. Next, the sample is rapidly heated to hydrothermal temperatures ( $T_H$ ) and pressures ( $P_H$ ) using computer-controlled microwave irradiation (MWI). A typical reaction time is 5 min (including heating and cooling times). After each layer ( $n$ ) deposition (heating cycle), a  $100 \mu\text{L}$  aliquot was collected for UV-vis and TEM analysis, and a fresh  $100 \mu\text{L}$  aliquot of 1 mM  $\text{AgNO}_3$  is added. Thus, the total [NP] is decreasing over the course of the reaction because of sampling. The process is then repeated an  $n$  number of times, resulting in the growth of the Ag-rich core/shell nanostructure. It is important to note that the expected growth is highly susceptible to NP size and concentration, as well as the volumes sampled during the course of shell addition. A plot of the expected growth, based on initial [NP], core diameter ( $d_c$ ),  $[\text{Ag}^+]$  added, and [NP] dilution, is shown in Figure 4a. The final Au/Ag products were stored in the reaction mother liquor and protected from light. Under these storage conditions, the Au/Ag NPs were stable indefinitely.

## INSTRUMENTATION

**Synthetic Microwave Reactor.** A Discovery-S (CEM Inc.) synthetic microwave reactor was employed. The instrument is

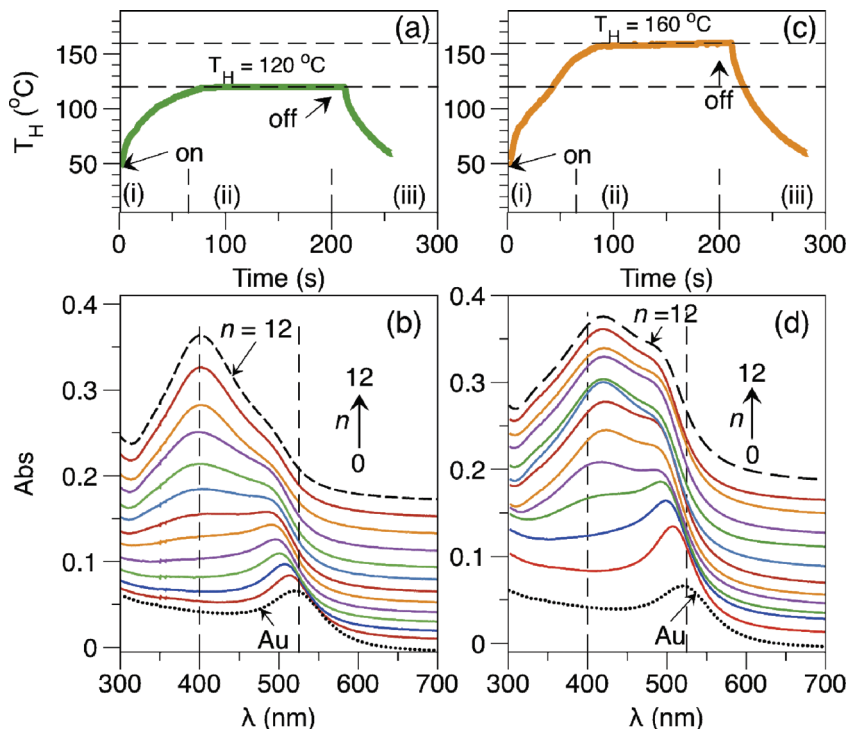


**Figure 2.** In situ temperature profiles at (a)  $T_H = 120\text{ }^\circ\text{C}$  and (c)  $T_H = 160\text{ }^\circ\text{C}$  and representative sets of UV-vis results for the Au/Ag NPs at increasing shell layers,  $n = 1-12$ , for (b)  $T_H = 120\text{ }^\circ\text{C}$  and (d)  $T_H = 160\text{ }^\circ\text{C}$ . The UV-vis spectra are offset for clarity.

computer-controlled and operates at power values between 0 and 300 W, temperatures ranging from 30 to 300  $^\circ\text{C}$ , and pressures from 0 to 200 psi. Temperature is monitored in situ during synthesis via the use of an integrated IR sensor, or via an immersed fiber optic temperature probe. The instrument is equipped with an active pressure monitoring system, which provides both pressure monitoring and added safety during synthesis. Taken together, this combination allows the MWI power to be dynamically attenuated by temperature feedback measured via the integrated infrared detector or fiber optic probe, allowing for fine control of annealing temperature, the ability to rapidly achieve hydrothermal conditions, and control of heating and cooling rates. Pressure-rated glass reaction vials with volumes of 10 or 35 mL were employed during synthesis. Active cooling was provided by the influx of the MW cavity with compressed  $\text{N}_2$ , which rapidly cools the sample at a controlled rate.

**UV-visible Spectrophotometry (UV-vis).** The UV-vis measurements were collected on a Varian Cary100 Bio UV-vis spectrophotometer between 200 and 900 nm. The instrument is equipped with an eight-cell automated holder with a high-precision Peltier heating controller.

**Transmission Electron Microscopy (TEM).** TEM measurements were performed on either an FEI T12 Twin TEM operated at 120 kV with a LaB6 filament and a Gatan Orius dual-scan CCD camera (Cornell Center for Materials Research) or a JEOL 2000EX instrument operated at 120 kV with a tungsten filament (SUNY-ESF, N.C. Brown Center for Ultrastructure Studies). Particle size was analyzed manually by modeling each particle as a sphere, with statistical analysis performed using ImageJ software on populations of at least 100 counts.

**High-Resolution Transmission Electron Microscopy (HRTEM).** HRTEM measurements were performed at the CCMR on an FEI T12 Spirit TEM/STEM operated at 120 kV

with a field emission source and a SIS Megaview III CCD camera. The instrument is equipped with both a bright-field and a dark-field HAADF STEM detector. The selective area energy-dispersive X-ray analysis (EDX) was performed in situ to STEM visualization, using an EDAX Genesis X-ray detector with internal elemental calibration.

**X-ray Photoelectron Spectroscopy (XPS).** XPS analysis was performed at the CCMR on Surface Science Instruments (SSI) model SSX-100 that utilizes monochromated aluminum  $\text{K}\alpha$  X-rays (1486.6 eV). The nanoparticles were drop-cast onto a silicon wafer and studied at an angle of 55°, which corresponds to an analysis depth of  $\sim 5$  nm. The data were processed using CasaXPS software. Before analysis, each sample was purified free of any excess metallic ions by centrifugation.

## ■ DISCRETE DIPOLE APPROXIMATION (DDA) MODELING

The NP and core/shell NP surface plasmon resonance (SPR) extinction spectra were modeled using the discrete dipole approximation (DDA) method developed by Draine and Flatau.<sup>45</sup> The open source software package DDSCAT 7.07<sup>45</sup> was employed on a Linux workstation equipped with an Intel i7 processor and 12 GB SDRAM running Ubuntu. Isotropic cores were calculated via the ELLIPSOID DDSCAT routine, whereas core/shell morphologies were calculated via the CONELLIPS routine with defined core diameters and shell thicknesses. Typical calculation times ranged from minutes for simple structures to 12–24 h for large diameters or complex core/shell geometries. In DDA (eq 1), a numerical SPR solution is defined by dividing an NP into elemental cubic volumes that are characterized by their coordinates within the NP, and their subsequent polarizability.<sup>42,45,46</sup> Thus, each unit can be treated

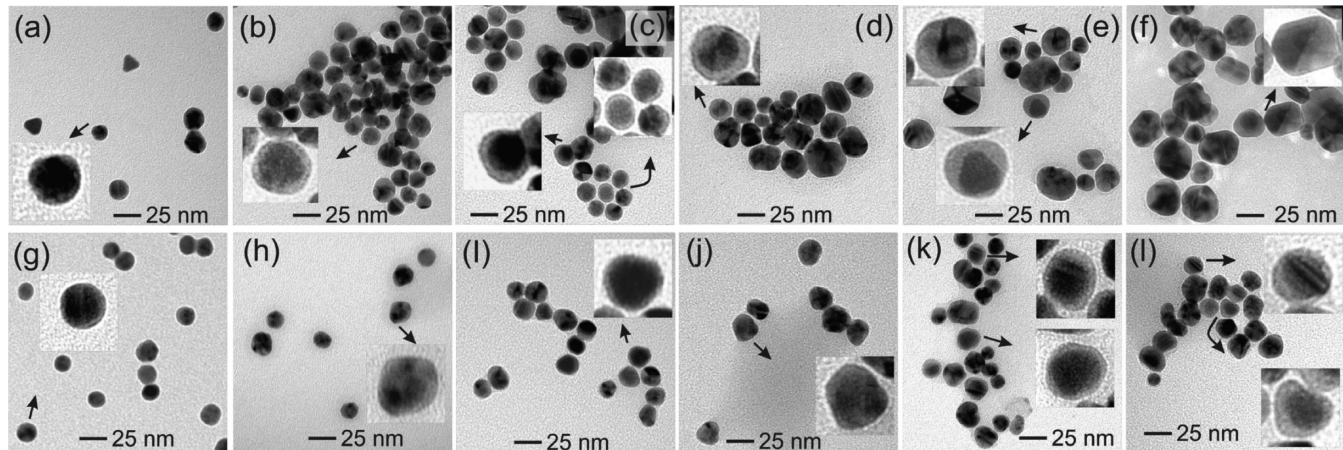


**Figure 3.** TEM results for Au/Ag fabricated at  $T_H = 120\text{ }^\circ\text{C}$  (a–f) and  $T_H = 160\text{ }^\circ\text{C}$  (g–l) for shell layers  $n = 3, 7, 10, 13, 17$ , and  $20$ . Statistical analysis (see Figures S2 and S3, Supporting Information) yields sizes of (a)  $n = 3, 17.9 \pm 1.8\text{ nm}$ , (b)  $n = 7, 19.5 \pm 2.3\text{ nm}$ , (c)  $n = 10, 22.6 \pm 3.3\text{ nm}$ , (d)  $n = 13, 24.9 \pm 5.0\text{ nm}$ , (e)  $n = 17, 26.0 \pm 7.1\text{ nm}$ , (f)  $n = 20, 33.5 \pm 6.3\text{ nm}$ , (g)  $n = 3, 17.1 \pm 1.9\text{ nm}$ , (h)  $n = 7, 20.3 \pm 2.3\text{ nm}$ , (i)  $n = 10, 20.4 \pm 2.2\text{ nm}$ , (j)  $n = 13, 20.7 \pm 2.4\text{ nm}$ , (k)  $n = 17, 21.9 \pm 1.9\text{ nm}$ , and (l)  $n = 20, 22.9 \pm 3.1\text{ nm}$ . Insets: magnified regions of interest at arbitrary scales. Original Au core shown in Figure S1 (Supporting Information) ( $n = 0, 15.4 \pm 0.7\text{ nm}$ ).

as a dipole, the collection of which has shown great accuracy in describing not just SP  $\lambda_{\max}$  but also the entire shape of the SP band (i.e., accurate NP mapping):

$$\sigma_{\text{ext}} = \frac{4\pi k}{|E_0|^2} \sum_{j=i}^N (\mathbf{E}_{\text{loc},j}^* \cdot \mathbf{P}_j) \quad (1)$$

Here, the SPR extinction ( $\sigma_{\text{ext}}, Q_{\text{ext}}$ ) is related to the sum of  $N$  discrete dipole vectors (fields)  $E^*$  and  $P_j$ , corresponding to electrical field and polarization, and  $k$  is a constant ( $k = m_0(2\pi/\lambda)$ ;  $m_0$  = related to the material index of refraction (eq 1). Wavelength-dependent dielectric tables for both Au and Ag were generated using well-established optical constants.<sup>70</sup> For the  $\text{Au}_x\text{Ag}_{1-x}$  solid solution alloys, we calculated dielectric constants for a binary alloy by linear combination of individual Au and Ag values, namely,  $\epsilon_{\text{Alloy}}(x, \lambda) = x_{\text{Ag}}\epsilon_{\text{Ag}}(\lambda) + (1 - x_{\text{Ag}})\epsilon_{\text{Au}}(\lambda)$ , where  $x_{\text{Ag}}$  is the volume fraction of Ag and  $\epsilon_{\text{Au}}$  and  $\epsilon_{\text{Ag}}$  are the wavelength-dependent dielectric constants for gold and silver, respectively. Such a method was recently described by El-Sayed and co-workers,<sup>34–36</sup> and some theoretical work has been done recently.<sup>49</sup> A similar approach was also used recently for alloy nanorods.<sup>50</sup> The  $\text{Au}_x\text{Ag}_{1-x}$  simulations were then employed for an alloy core and core/alloy DDA calculations.

## RESULTS

By processing at hydrothermal temperatures ( $T_H$ ) using MWI, highly controllable and unique optical and morphological properties emerge from the Au/Ag system. At  $T_H = 120\text{ }^\circ\text{C}$  (Figure 2a), we observed a colorimetric change from the ruby-red color of the AuNP to a reddish-orange after only one layer ( $n = 1$ ), then gradually to orange at  $n = 3–5$ . Ultimately, the color evolves to dark yellow at increased shell layers ( $n > 5$ ). Importantly, the solution itself remains optically clear and stable, suggesting growth of the new Ag-rich nanostructure and lack of aggregation. Control experiments subjecting the Au to these conditions without  $\text{AgNO}_3$  addition resulted in a stable Au SPR with no change to morphology or concentration. To follow this transformation, we employed UV-vis and transmission electron microscopy (TEM).

The SPR progression at  $T_H = 120\text{ }^\circ\text{C}$  shown in Figure 2b reveals three distinct features that are a function of shell type, thickness, and temperature. First, at the initial shell layers ( $n = 1–4$ ), we observe a novel blue shift of the SPR wavelength ( $\lambda_{\text{SPR}}$ ) from 522 to 498 nm. Second, the  $\lambda_{\text{SPR}}$  shift is subsequently followed by the growth of a second SPR centered at  $\approx 400\text{ nm}$ . Third, the SPR at 400 nm increases in extinction at  $n > 5$ , with a slight red shift consistent with the growth of a larger Ag NP. This SPR response is qualitatively in agreement with the formation of a Ag-rich nanostructure.<sup>34–42</sup> However, a close investigation of the SPR characteristic indicates a more intriguing two-step growth mechanism of the Au/Ag particles. For instance, the initial blue shift in  $\lambda_{\text{SPR}}$  from 522 to 498 nm, as well as the single-peak nature of its SPR, strongly suggests not simply the formation of a phase-segregated core/shell nanostructure but the initial formation of a  $\text{Au}_x\text{Ag}_{1-x}$  alloy skin.

It has been shown that the  $\lambda_{\text{SPR}}$  for a binary  $\text{Au}_x\text{Ag}_{1-x}$  NP is linearly correlated to composition,<sup>34–42</sup> with higher Ag concentrations exhibiting blue shifted SPR. Importantly, such solid-solution alloys are known to maintain single SPR characteristics. For instance, El-Sayed and co-workers have synthesized  $\text{Au}_x\text{Ag}_{1-x}$  and showed a near linear SPR for particles of similar core sizes.<sup>34–36</sup> As well, Murphy and co-workers investigated the SPR response to alloy composition and revealed that a physical mixture of Au and Ag NPs cannot account for such an SPR response.<sup>47</sup> In addition, the spontaneous alloying of AuAg NPs with  $d < 5\text{ nm}$  showed a composition-dependent SPR.<sup>38–40</sup> The extent of the shift, as well as the extinction, is further related to size and shape. The blue shift of a single SPR band observed in Figure 2b for the initial layers ( $n = 1–4$ ) largely follows this alloy trend. In the second step, an increasingly thick Ag shell is grown, which results in the sequential growth of a  $\lambda_{\text{SPR}}$  centered at  $\approx 400\text{ nm}$ , further shielding the core and alloy intermediate shell, resulting in the shoulder at  $\approx 490\text{ nm}$ . At thicker shells at  $n > 11$ , only a single SPR is observed at  $\approx 410\text{ nm}$  (Figure S2, Supporting Information).

This optical behavior was correlated with morphology change using TEM (Figure 3), which confirmed the growth of Au/Ag NPs as a function of deposition layer,  $n$ . From an initial AuNP with  $d_C = 15.4 \pm 0.7\text{ nm}$ , a growth to core + shell diameters,

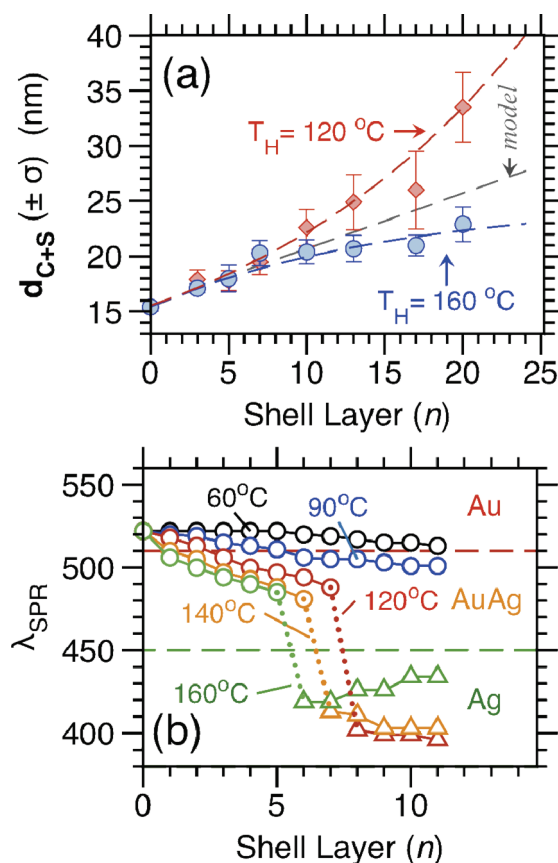


**Figure 4.** (a) A summary of the Au/Ag diameter ( $d_{C+S}$ ) increase with shell layer ( $n$ ) at both  $T_H = 120$  and  $160\text{ }^\circ\text{C}$ . Error bars represent the  $d_{C+S}$  standard deviation ( $\sigma$ ). A model plot of the expected growth is shown for comparison and is based on the spherical growth of a Ag shell at the initial Au core and takes into account the dilution of [NP] at each  $n$  due to sampling for UV-vis and TEM. The  $d_{C+S}$  growth trends were fitted to the equations  $y = y_0 + A \exp(bx)$ ,  $b = 0.053$ , and  $y = y_0 + A \exp(-bx)$ ,  $b = 0.063$ , at  $T_H = 120$  and  $160\text{ }^\circ\text{C}$ , respectively, to guide the eye. (b) The summary of  $\lambda_{SPR}$  dependence on shell layer ( $n$ ) and processing at  $T_H = 60, 90, 120, 140$ , and  $160\text{ }^\circ\text{C}$ , indicating the transition (•••) from Au-SPR to Au/ $\text{Au}_x\text{Ag}_{1-x}$ -SPR (○), and to Ag-rich Au/ $\text{Au}_x\text{Ag}_{1-x}$ /Ag-SPR (Δ).

$d_{C+S} = 17.9 \pm 1.8$  (a),  $19.5 \pm 2.3$  (b),  $22.6 \pm 3.3$  (c),  $24.9 \pm 5.0$  (d),  $26.0 \pm 7.1$  (e), and  $33.5 \pm 6.3$  nm (f) was measured for  $n = 3, 7, 10, 13, 17$ , and  $20$ , respectively at  $T_H = 120\text{ }^\circ\text{C}$ . It is interesting to note that the Au/Ag maintain high monodispersity values at  $n = 1–4$  but become increasingly polydisperse at larger  $n$  (thicker  $t_s$ ), especially at  $n > 11$  (Figure S2, Supporting Information). A close inspection of the TEM images (see insets) reveals that a high percentage of the NPs show clear core/shell structures, especially at  $n > 7$ , and that shell growth does possess some dispersity and anisotropy in terms of the core position and shell thickness.

As hypothesized, the SPR response,  $d_{C+S}$ , and alloy formation were found to be highly susceptible to processing  $T_H$ . Figure 2d shows the UV-vis profile of Au/Ag prepared under identical conditions except a raise to  $T_H = 160\text{ }^\circ\text{C}$ . Such a temperature increase and control was trivial using our MWI-based method, as shown by the temperature profiles (Figure 2c). Compared to the Au/Ag processed at  $120\text{ }^\circ\text{C}$ , we observe a new SPR signature. A major characteristic of this difference is the significant shoulder

observed at  $\approx 480\text{ nm}$ , along with a second  $\lambda_{SPR}$  centered at  $\approx 425\text{ nm}$ . Interestingly, the  $T_H = 160\text{ }^\circ\text{C}$  system exhibits only a minimal increase in extinction coefficient, as expected for a more alloy-rich shell (Figures S3 and S7, Supporting Information). These results suggest either a larger role of Au in the new nanostructure or the presence of a thick alloy intermediate layer, as compared to the previous  $T_H = 120\text{ }^\circ\text{C}$  case.

The TEM micrographs for Au/Ag prepared at  $T_H = 160\text{ }^\circ\text{C}$  are shown in Figure 3g–l (lower panel). We observed two main differences when compared with  $T_H = 120\text{ }^\circ\text{C}$  (top panel). First, samples prepared at elevated  $T_H$  show improved monodispersity and smaller sizes at high  $n$ . Second, the visualization of a core/shell morphology is largely limited to  $n > 11$ , which suggests a higher degree of alloying at intermediate layers as a result of the  $T_H$  increase (see below). Figure 4 summarizes these TEM and SPR observations by showing the relationship between  $d_{C+S}$  (a) and  $\lambda_{SPR}$  shift (b) with  $n$  and processing  $T_H$ . Interestingly, the NPs show very similar  $d_{C+S}$  up to  $n \sim 7$ , which then diverge in a counterintuitive trend at  $n > 7$  (Figure 4a). Larger and more polydisperse  $d_{C+S}$  are observed at  $T_H = 120\text{ }^\circ\text{C}$ , whereas NPs prepared at  $T_H = 160\text{ }^\circ\text{C}$  show smaller diameters and improved monodispersity (as represented by error bars). When compared to a plot of ideal growth (Figure 4a), based on [NP],  $[\text{Ag}^+]$ ,  $d_C$ , and [NP] dilution, both systems show nonideal growth, suggesting different growth models to be at play (vide infra). The  $\lambda_{SPR}$  shift was also found to be highly sensitive to  $T_H$  (Figure 4b), with increased  $T_H$  resulting in a more rapid initial SPR blue shift. On the other hand, control experiments at  $T_H < 100\text{ }^\circ\text{C}$  suggest much slower alloy diffusion or shell growth, as evidenced by a minimal  $\lambda_{SPR}$  blue shift (Figure 4b).

Evidence of Ag shell growth and core/shell structure was provided by high-resolution TEM (HRTEM) and scanning TEM (STEM) in combination with selective area energy-dispersive X-ray analysis (EDX). Figure 5a shows a representative STEM image for typical Au/Ag prepared at  $T_H = 120\text{ }^\circ\text{C}$  and  $n = 10$ . HRTEM images of selected Au/Ag (Figure 5b,c) show a clear core/shell morphology with dimensions that agree well with the growth mechanism and protocol design (Figure 1). The NP composition was probed by selective area EDX and obtained for a single NP (Figure 5d) and a grouping (Figure 5e) of NPs that provide clear evidence of both Au and Ag L-edge binding energies at  $\approx 2.1$  and  $\approx 3.0$  keV, respectively. The quantitative analysis of the EDX reveal a Au/Ag composition ratio of 1:0.95 and 1:1.06, respectively. Compositional changes were also observed by X-ray photoelectron spectroscopy (XPS). For example, at shell  $n = 7$ , XPS revealed a Au/Ag composition of 14:86 and 19:81 for  $T_H = 120$  and  $160\text{ }^\circ\text{C}$ , respectively (Table S1, Supporting Information). At  $n = 7$ , both NPs show similar  $d_{C+S}$  (Figure 4b), suggesting an increased Au content in the shell itself. At the XPS analysis angles employed ( $55^\circ$ ), we can expect a penetration depth of  $\sim 5$  nm, suggesting that a considerable portion of the core will contribute to the observed stoichiometry, because shell thicknesses for these samples are  $t_s \approx 2$  nm.

We further utilized chemical means to decipher the core/shell and core/alloy/shell structure of the NPs by selective etching of Ag. For this, the ligand bis(*p*-sulfonatophenyl)phenylphosphine (BSPP) was employed. BSPP has been shown to oxidize Ag by formation of a BSPP– $\text{Ag}^+$  but cannot oxidize Au.<sup>16</sup> For instance, when added at high concentration ratios ( $[\text{BSPP}]/[\text{NP}] > 100\,000$ ), we observed the immediate change in color of the Au/Ag solutions from yellow/orange to red, suggesting the removal of the Ag-rich shell and resulting in the original Au

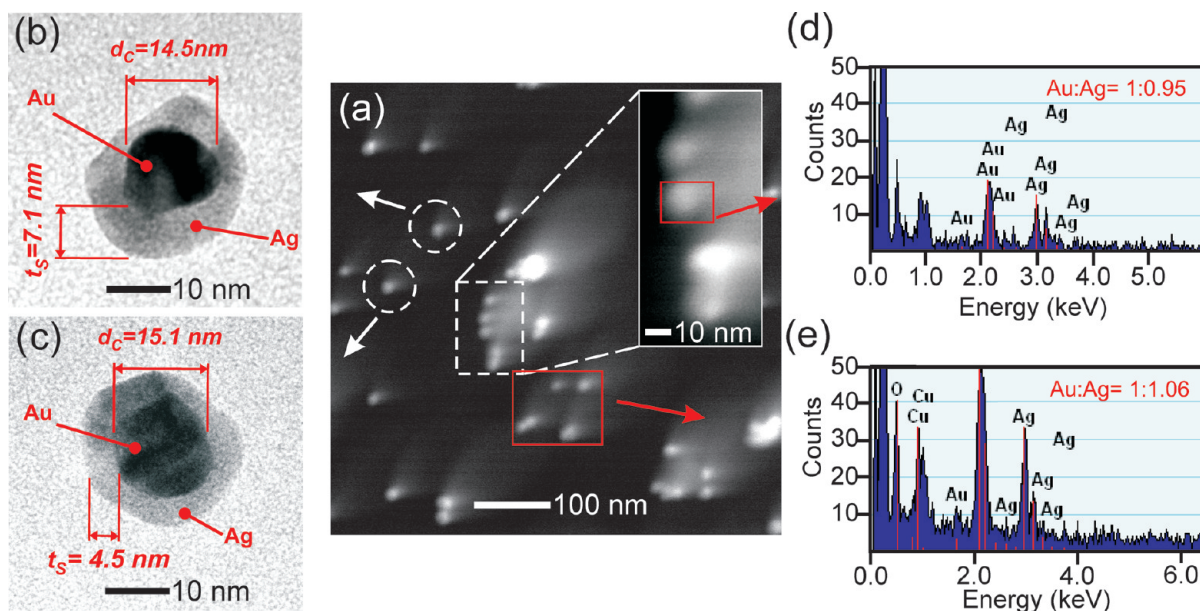


**Figure 5.** (a) A representative STEM micrograph of the Au/Ag NP prepared at  $n = 10$  and  $T_H = 120$   $^{\circ}\text{C}$ . (b, c) HRTEM micrographs of individual Au/Ag NPs. (d, e) Corresponding selected area EDX spectra for the regions outlined for a single NP and a group of five NPs, revealing the presence of both Au and Ag within the NP itself.

core. This shell etching was followed via UV-vis (Figure S5, Supporting Information). The Au/Ag prepared at  $T_H = 120$   $^{\circ}\text{C}$  showed a nearly  $\sim 10\times$  increase in etching kinetics compared with the  $T_H = 160$   $^{\circ}\text{C}$  sample, suggesting a pure Ag shell and AuAg alloy shell, respectively. Examination via TEM revealed a decrease in core diameter to values similar to the initial Au core in both systems. Interestingly, the resulting etching leads to SPR trends in close agreement with the reverse of the layer-by-layer growth (Figure S5, Supporting Information).

Taken together, these results show that the layer-by-layer deposition of Ag shells at Au NP cores leads to optical and morphological characteristics that are highly temperature-dependent. These observations suggest an alloy formation at the core interface, whose interdiffusion rate is susceptible to the temperatures employed, which may ultimately lead to two competing growth mechanisms. We next discuss these potential findings by first modeling the resulting SPR behavior with a series of core/shell and core/alloy/shell models using discrete dipole approximation (DDA) and then describe the contrasting shell growth mechanisms observed, as well as the potential for local heating at the NP interface resulting from the use of MWI as a heating source.

An intriguing fundamental aspect of this system is the significant change in SPR response (Figure 2), from relatively minor changes to NP size and shape (Figure 3). Thus, the internal structure and composition of the core/shell or core/alloy/shell are critical for the SPR. Figure 1a shows the composition and morphological parameters that tailor SPR. The core of known diameter ( $d_C$ ) and wavelength-dependent dielectric constant ( $\epsilon_C$ ) is encased in a shell of a second material ( $\epsilon_S$ ) with a fine-tuned thickness ( $t_S$ ) and surrounded by a dielectric medium ( $\epsilon_M$ ). The influence of the immediate ligand shell and local ionic strength is not accounted for at this time. To gain deeper insights into the relationship between the observed SPR and particle morphology, we employed DDA.<sup>45</sup> In DDA, a numerical solution is defined by dividing an NP into elemental cubic volumes that are characterized by their coordinates within the NP, and

their subsequent polarizability.<sup>45,46</sup> Thus, each unit can be treated as a dipole, the collection of which has shown great accuracy in describing not just SPR  $\lambda_{\text{max}}$  but also the entire shape of the SPR band. Such treatment is critical for increasingly complex plasmonic structures and has been employed recently to explore triangular silver nanoprisms and nanostructures,<sup>46</sup> as well as AuAg nanoboxes.<sup>48</sup>

Figure 6 shows a series of DDA calculations for an idealized phase-segregated core/shell (a), as well as a core/alloy NP (b, c). For a spherical AuNP with  $d_C = 10.0$  nm and an increasing number of concentric Ag shells with  $t_S = 0.25, 0.50, 0.75$ , and  $1.0-7.0$  nm, the simulations reveal a significant  $\lambda_{\text{SPR}}$  blue shift, with the immediate emergence of a second Ag-based SPR at  $\approx 390$  nm (Figure 6a). An increase in  $t_S$  from 1.0 to 7.0 nm results in screening of the Au core and a predominantly Ag SPR that shows a subtle red shift with increasing thickness.<sup>42</sup> A closer look at the subnanometer shell thickness,  $t_S = 0.25$  and  $0.50$  nm (Figure 6a, inset), shows an intermediate  $\lambda_{\text{SPR}}$  shift, but still accompanied by a second  $\lambda_{\text{SPR}}$  at  $\approx 350$  nm. These core/shell simulations show two key characteristics: (i) the existence of two SPRs is confirmed, one attributed to the core, and the second to the shell, and (ii) that the increasing shell thickness in the phase-segregated model is clearly in agreement with the experimental trends at high  $n$  (Figures 2b and S2, Supporting Information).<sup>42</sup> However, the results cannot completely replicate the experimental observations of the initial  $\lambda_{\text{SPR}}$  blue shift of a single SPR, such as that observed for  $n = 1-4$ , nor the overall SPR response for the  $T_H = 160$   $^{\circ}\text{C}$  system (Figure 2c), suggesting formation of an intermediate  $\text{Au}_x\text{Ag}_{1-x}$  alloy layer of varied composition and/or thickness.

To investigate this postulated alloy shift, we performed similar DDA calculations using an alloy (Figure S4, Supporting Information) and core/alloy model (Figure 6b,c). Alloy simulations for a  $d_C = 10.0$  nm  $\text{Au}_x\text{Ag}_{1-x}$  binary NP of  $x = 0.05, 0.15, 0.25, 0.35, 0.50, 0.70$ , and 1.0 were first performed (Figure S4, Supporting Information). For this, we calculated dielectric

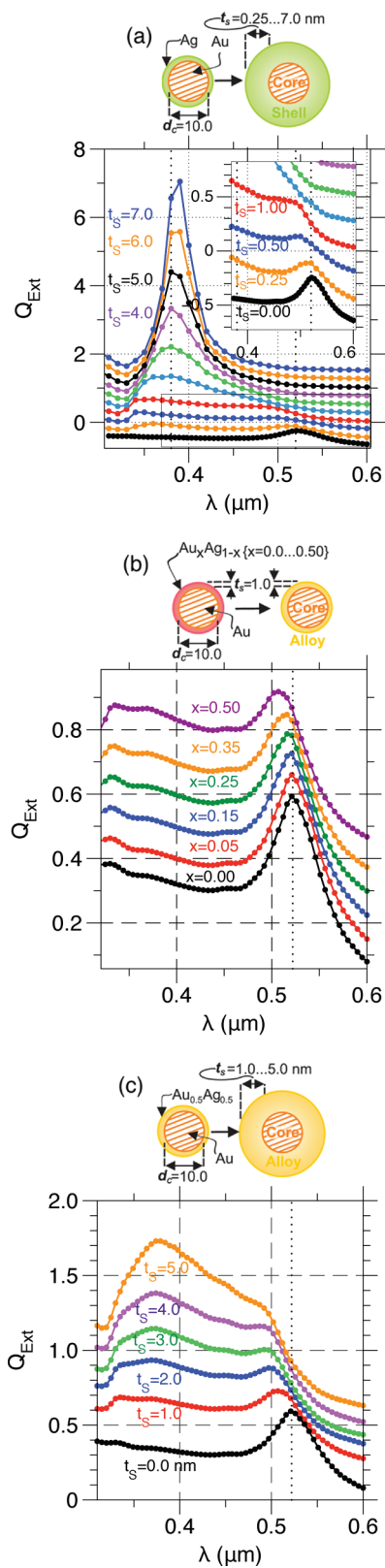


**Figure 6.** (a) DDA simulations for phase-segregated Au/Ag core/shell NPs with Au  $d_C = 10.0$  nm and Ag  $t_S = 1.0, 2.0, 3.0, 4.0$ , and  $5.0$  nm. Inset: magnified region of interest for thin shell regions ( $t_S = 0.25, 0.50, 1.0$  nm). (b) DDA simulations for Au/ $Au_xAg_{1-x}$  core/alloy NPs at fixed  $t_S = 1.0$  nm and  $x = 0.00, 0.05, 0.15, 0.25, 0.35$ , and  $0.50$ . (c) DDA simulations for Au/ $Au_xAg_{1-x}$  core/alloy with  $x = 0.50$  and varied  $t_S = 1.0, 2.0, 3.0, 4.0$ , and  $5.0$  nm. The surrounding dielectric medium is water, and spectra are offset for clarity only.

constants for a binary alloy by linear combination of individual Au and Ag values, namely,  $\varepsilon_{\text{Alloy}}(x, \lambda) = x_{\text{Ag}}\varepsilon_{\text{Ag}}(\lambda) + (1 - x_{\text{Ag}})\varepsilon_{\text{Au}}(\lambda)$ , where  $x_{\text{Ag}}$  is the volume fraction of Ag and  $\varepsilon_{\text{Au}}$  and  $\varepsilon_{\text{Ag}}$  are the wavelength-dependent dielectric constants for gold and silver, respectively. Such a method was recently described by El-Sayed and co-workers,<sup>34–36</sup> and some theoretical work has been done recently.<sup>49</sup> A similar approach was also used recently for alloy nanorods.<sup>50</sup> The  $Au_xAg_{1-x}$  simulations were then employed for a core/alloy DDA calculation.

Figure 6b shows the modeled effect of a Au/ $Au_xAg_{1-x}$  core/alloy NP with a fixed  $t_S = 1.0$  nm and varied alloy composition,  $x = 0.00, 0.05, 0.15, 0.25, 0.35$ , and  $0.50$ . The resulting DDA spectra reveal a subtle blue shift in  $\lambda_{\text{SPR}}$ , the magnitude of which is linearly dependent on the fraction of Ag in the 1 nm shell. Moreover, the spectra maintain the single SPR nature. This shift is consistent with that experimentally observed at  $n = 1–4$  for both  $T_H = 120$  and  $160$  °C, again indicating the formation of an alloy layer. We further investigated the effect of an alloy shell by simulating a Au/ $Au_{0.5}Ag_{0.5}$  NP with a  $d_C = 10.0$  nm Au core with an increasing alloy shell thickness of  $t_S = 1.0–5.0$  nm (Figure 6c). The simulation shows intriguing results that are consistent with the experimental data, namely, the intermediate  $\lambda_{\text{SPR}}$  blue shift of a single SPR resonance, particularly up to  $t_S = 1.0–2.0$ . It is also interesting to note that the thick alloy shell SPR shown in Figure 6c qualitatively agrees very well with those experimentally observed (Figure 2). This strongly reinforces the idea of an increased alloy layer thickness as a function of both  $n$  and  $T_H$ . The subtle differences between the experimental UV-vis and the DDA plasmon modeling can be attributed to variation between the experimental and model NP dimensions ( $d_C$ ), such as anisotropy effects, polydispersity, and the high likelihood of the intermediate alloy layer possessing a compositional gradient between the Au-rich core and the Ag shell, as well as potential dielectric effects. On the other hand, these results and modeling suggest the exciting possibility that, by controlling core/shell dimensions and alloy layering, researchers can tune the plasmon response toward specific application goals. Furthermore, this also suggests that alloy compositions, morphology, or potential phase segregation can be explored and modeled by the SPR response itself, which is part of our ongoing work.

## DISCUSSION

In addition to the temperature-dependent plasmon response that is associated with these Au/Ag NPs, a second intriguing observation is the temperature-dependent growth observed. For instance, at  $T_H = 120$  °C, the  $d_{C+S}$  increase can best be fit to an exponential growth, as shown by the fitting in Figure 4a. These NPs also show increased polydispersity at  $n > 10$ . In contrast, the NPs prepared at  $T_H = 160$  °C have smaller overall  $d_{C+S}$ , consistent size distributions, and a decreased rate of growth at  $n > 10$ . Because both systems follow the same synthesis design and share identical concentrations and precursor batches, this relationship between shell growth and  $T_H$  suggests a large mechanistic shift. This is further illustrated by a comparison to a plot of ideal shell growth based on the availability of  $Ag^+$  and [NP] at each  $n$ , as shown in Figure 4a. Although more studies are needed to fully elucidate the mechanism, we believe we are observing a competition between interfacial alloying at the high temperature regime (HT,  $T_H = 160$  °C) and an interfacial ripening at the low-temperature regime (LT,  $T_H = 120$  °C).

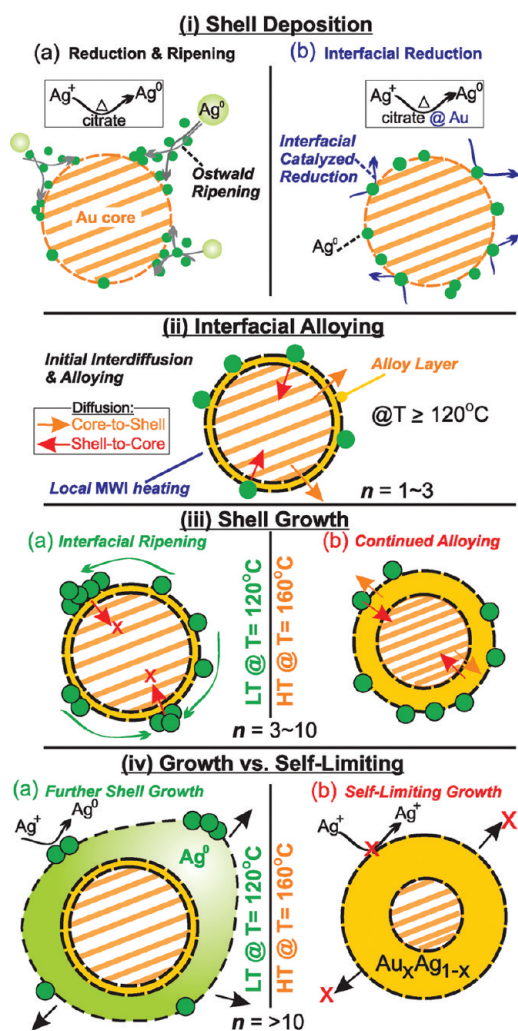


**Figure 7.** Proposed growth mechanism for the core/alloy/shell NPs. Shell growth is initiated (i) by either an Ostwald ripening of nucleated shell materials (i-a) or a core catalyzed interfacial reduction (i-b). Upon initial shell deposition (ii), a thin skin of alloy is formed, which is observed only at  $T_H \geq 120$  °C. Next, shell growth (i.e., layers,  $n$ ) behavior is dominated by a low-temperature (LT,  $T_H = 120$  °C, iii-a) or a high-temperature (HT,  $T_H \geq 160$  °C, iii-b) growth regime and transition. At LT, alloy interdiffusion is limited, and alloying competes with interfacial ripening of the deposited shell (iii-a). Upon additional layers, the LT growth results in further ripening, leading to an exponential increase in diameter at high  $n$  (Figure 4a) and increased polydispersity (iv-a). At HT, alloy interdiffusion between the deposited shell and core metals is much improved and thus limits interfacial ripening (iii-b). At high  $n$ , the NP has a rich alloy composition, which limits further shell growth and also disrupts any interfacial catalytic reduction of  $\text{Ag}^+$  (iv-b). This results in a self-limiting growth regime (Figure 4a).

Our proposed mechanism is illustrated in Figure 7. In brief, the growth of either a monometallic Ag shell or an alloy shell is first related to the deposition of a thin Ag shell ( $n = 1-3$ ), with a thickness controlled by  $n$  (step i). This shell deposition takes place either by a solution-phase Ostwald ripening<sup>51,52,62</sup> of small Ag NPs initially nucleated (i-a) or via a surface catalytic reduction of  $\text{Ag}^+$  at the Au interface (i-b). Once a layer of Ag is deposited on the Au core, the Ag atoms undergo spontaneous alloying and interdiffusion, the depth and composition of which

is proportional to core size and  $T_H$  (step ii, see below).<sup>29,61</sup> Here, we note that alloying, as observed from the SPR blue shift, was only observed at  $T_H \geq 120$  °C for our core diameter (Figure 4b).<sup>29</sup> Upon the formation of the alloy skin, there are then two competing growth mechanisms leading to the observed optical properties, growth characteristics, and size distribution at  $n = 3-10$  (step iii). These two pathways include either the LT interfacial ripening of the continuously deposited Ag, ultimately leading to a monometallic shell (iii-a), or the HT interfacial interdiffusion resulting in a thick alloy shell (iii-b). These contrasting growth mechanisms are further evident at high shell layers,  $n > 10$  (iv), where the LT system shows further shell growth due to simple reduction and ripening (iv-a), whereas the HT system shows a self-limiting behavior due to its continued alloy interdiffusion, and subsequent compositional changes (iv-b). In addition, any interfacial catalyzed reduction of  $\text{Ag}^+$  (i-b) may also be energetically diminished by the decreased surface tension at the alloy interface.<sup>58</sup> Multiple control experiments in which the Au/Ag prepared at  $T_H = 160$  °C at  $n = 10$  were further processed in the presence of a high excess of  $[\text{Ag}^+]$  yielded little to no growth, confirming that available  $\text{Ag}^+$  is not the primary consideration for growth. Moreover, the use of elevated  $T_H$ , up to 210 °C, also showed similar limited growth characteristics and increased alloying. These studies are currently underway and will be reported elsewhere.

Such an example of a self-limiting growth phenomenon is not often observed in nanosystems, due, in large part, to the typical free energy gains of ripening.<sup>51,52,62</sup> Interestingly, self-limiting behavior is indeed a characteristic of bulk metal alloys that undergo interchange mechanisms as the primary diffusion pathway,<sup>51,52</sup> particularly at solid–liquid interfaces, such as at temperatures near respective melting points. For example, bulk alloys can show a unique, order–disorder phase transition, with varied degrees of short- or long-range ordering. These second-order phase transitions, often termed lambda transitions, are found in classical alloys, such as  $\beta$ -brass ( $\text{CuZn}$ ).<sup>51</sup> In brief, a lambda transition is observed when an optimal alloy ratio is achieved for a given temperature at a solid–liquid interface. Here, alloy formation contributes to free energy gain by the negative heat of formation (e.g., enthalpic gain) for miscible alloys,<sup>61</sup> as well as the realization of an optimal composition that is related to the maximum distribution of the alloy (e.g., highest configurational entropy) for a given crystal type at a critical temperature ( $T_C$ ).<sup>51,52</sup> This entropic contribution, in particular, increases until a maximum randomness of alloy composition is achieved via interchange. Once met, further alloying is less favorable, and thus decreased compositional change occurs. Both energetic gains are known to be highly size-dependent, as are kinetic considerations related to diffusion coefficient changes from core to shell and shell to core, depending on interfacial area and relative layer thicknesses.<sup>61</sup> Thus, the thermodynamics of the order–disorder systems are known to be self-limiting and highly cooperative. Because our NP interface will undoubtedly show size-dependent properties and because the interface is defect-rich, the present system provides a perfect condition for such alloy phase behavior to be observed at the nanoscale.

Indeed, such order–disorder transitions have only recently begun to be investigated via high-temperature annealing of magnetic alloy nanoparticles under TEM and XRD observations.<sup>53–60</sup> For example, the  $\text{A}_1\text{--Ll}_0$  phase transition has been investigated in  $\text{CoPt}$ ,<sup>53,54</sup>  $\text{FeCo}$ ,<sup>60</sup>  $\text{FePt}$ ,<sup>55</sup>  $\text{FePd}$ ,<sup>56</sup> and  $\text{AuPd}$ .<sup>57</sup> A number of recent Monte Carlo simulations have also investigated

nanoparticles with varied alloy compositions,<sup>59</sup> as well as interesting stabilization effects of alloy formation at the interfacial grain boundaries, which may improve nanoparticle stability.<sup>58</sup> Moreover, the energetic considerations of alloy formation at the nanoscale is also gaining attention, with recent work modeling in detail both the size-dependent thermodynamic and kinetic considerations.<sup>61</sup>

In addition to energetic considerations, our use of MWI as a dielectric heating source will likely induce a unique thermal nonequilibrium condition, which will introduce local heating at the Au NP interface.<sup>63–66</sup> Here, the metal NP itself will directly absorb MWI (100–150 W, 2.45 GHz) irradiation at a different rate than the surrounding medium (e.g., solvent).<sup>43,44,67–69</sup> We can expect that this nonequilibrium condition will result in the Au NP surface to be at a considerably higher  $T$  than the bulk solution (e.g., 120, 160 °C). This is particularly interesting from the standpoint of the present system, as it will undoubtedly influence both kinetic and thermodynamic considerations described above and may increase the NP interface above that of its melting point, which is possible because nanoscale melting temperature is drastically decreased at nanometer grain sizes.<sup>36</sup> This may allow for a liquid-skin formation, which is the favorable condition for alloying.<sup>61</sup> A more conclusive example of this effect was observed by Hartland and co-workers for the alloying of Au/Ag and Ag/Au via laser irradiation.<sup>39</sup> Their laser-induced heating and alloying, as observed via SPR change and TEM, was found to be dependent upon the local temperature of the nanoparticle. Such local heating was found to be related to the difference in heat dissipation between picosecond and nanosecond pulse rates.<sup>39</sup> The direct probing of nonequilibrium effects for MWI-based heating is also challenging and under intense investigation by us as well as others. For example, Wada and co-workers recently developed an experimental setup to probe the local heating phenomena at metal surfaces under MWI irradiation using single-molecule Raman probing.<sup>64</sup> Our future work will investigate this thermally induced alloy formation at presynthesized NP cores,<sup>71</sup> study both miscible and nonmiscible binary and ternary alloys, and further probe the MWI-induced alloying as a function of core size.

## CONCLUSIONS

In summary, we have shown the ability to deposit Ag shells of controlled thicknesses at presynthesized Au NP cores. The growth, optical properties, and morphology were found to be highly susceptible to the hydrothermal processing temperature employed, which was automated using MWI as a dielectric heating source. The shell growth proceeds under a core/alloy/shell growth mechanism, which was tailored by temperature, suggesting an atomic diffusion and alloying mechanism to be at play. Moreover, a shift in growth mechanism from a classical ripening model at low temperature to a self-limiting alloy transition at high temperature was observed. Here, self-limiting growth was observed by a decreased rate of growth for the nanoparticles when processed at high temperature, as opposed to an exponential growth at low temperature. This may be due to improved alloy interdiffusion at the high-temperature condition, suggesting an order-disorder transition. Moreover, the origin of the plasmon response of the core/alloy/shell nanoparticle was probed using DDA modeling, which showed the plasmon resonance to be sensitive to shell thickness and alloy composition. This processing approach, as well as the self-limiting alloy growth model, may

allow for high-fidelity control of a particle's size, interfacial composition, or plasmonic response without significantly altering the morphology. In addition, when further investigated, the interfacial alloying approach may lead to core/alloy nanostructures with tailored phase behavior, controlled growth, and improved resistance to interfacial ripening. Moreover, this approach may provide a useful platform on which to study nanoscale-alloying effects and phase behavior, which have been proposed theoretically. Furthermore, the particles will also find future utility as plasmonic antenna, metamaterials, optical probes, and surface enhanced Raman substrates.

## ASSOCIATED CONTENT

**S Supporting Information.** Figures S1–S7. This material is available free of charge via the Internet at <http://pubs.acs.org>.

## AUTHOR INFORMATION

### Corresponding Author

\*E-mail: mmmaye@syr.edu.

### Author Contributions

<sup>§</sup>These authors contributed equally to this work.

## ACKNOWLEDGMENT

We thank the Department of Chemistry and the Syracuse Biomaterials Institute (SBI) for generous start-up support. This work is partially supported by a Department of Defense PECASE award, sponsored by AFOSR (FA9550-10-1-0033). We acknowledge instrumentation access provided by the Cornell Center for Materials Research (CCMR, NSF/DMR 0520404), SUNY-ESF, and the Center for Functional Nanomaterials at Brookhaven National Laboratory (US-DOE DE-AC02-98CH10886).

## REFERENCES

- (1) Murray, C. B.; Norris, D. J.; Bawendi, M. G. *J. Am. Chem. Soc.* **1993**, *115*, 8706–8715.
- (2) Brust, M.; Walker, M.; Bethell, D.; Schiffrin, D. J.; Whyman, R. *Chem. Commun.* **1994**, 801–802.
- (3) Brennan, J. G.; Siegrist, T.; Carroll, P. J.; Stuczynski, S. M.; Brus, L. E.; Steigerwald, M. L. *J. Am. Chem. Soc.* **1989**, *111*, 4141–4143.
- (4) Alivisatos, A. P. *J. Phys. Chem.* **1996**, *100*, 13226–13239.
- (5) Mews, A.; Eychmuller, A.; Giersig, M.; Schooss, D.; Weller, H. *J. Phys. Chem.* **1994**, *98*, 934–941.
- (6) Schmid, E. G. *Clusters and Colloids*; VCH: Weinheim, Germany, 2004.
- (7) Daniel, M. C.; Astruc, D. *Chem. Rev.* **2004**, *104*, 293–346.
- (8) Gole, A.; Murphy, C. J. *Chem. Mater.* **2004**, *16*, 3633–3640.
- (9) Murphy, C. J.; San, T. K.; Gole, A. M.; Orendorff, C. J.; Gao, J. X.; Gou, L.; Hunyadi, S. E.; Li, T. *J. Phys. Chem. B* **2005**, *109*, 13857–13870.
- (10) Peng, X. G.; Wickham, J.; Alivisatos, A. P. *J. Am. Chem. Soc.* **1998**, *120*, 5343–5344.
- (11) Mokari, T.; Sztrum, C. G.; Salant, A.; Rabani, E.; Banin, U. *Nat. Mater.* **2005**, *4*, 855–863.
- (12) Habas, S. E.; Lee, H.; Radmilovic, V.; Somorjai, G. A.; Yang, P. *Nat. Mater.* **2007**, *6*, 692–697.
- (13) Talapin, D. V.; Mekis, I.; Gotzinger, S.; Kornowski, A.; Benson, O.; Weller, H. *J. Phys. Chem. B* **2004**, *108*, 18826–18831.
- (14) Prodan, E.; Radloff, C.; Halas, N. J.; Nordlander, P. *Science* **2003**, *302*, 419–422.

- (15) Wang, H.; Brandl, D. W.; Le, F.; Nordlander, P.; Halas, N. J. *Nano Lett.* **2006**, *6*, 827–832.
- (16) (a) Xue, C.; Metraux, G. S.; Millstone, J. E.; Mirkin, C. A. *J. Am. Chem. Soc.* **2008**, *130*, 8337–8344. (b) Tan, Y. N.; Yang, J.; Lee, J. Y.; Wang, D. I. C. *J. Phys. Chem. C* **2007**, *111*, 14084–14090.
- (17) Zhang, Q. B.; Xie, J. P.; Lee, J. Y.; Zhang, J. X.; Boothroyd, C. *Small* **2008**, *4*, 1067–1071.
- (18) Skrabalak, S. E.; Xia, Y. *ACS Nano* **2009**, *3*, 10–15.
- (19) Sun, Y. G.; Xia, Y. *Nano Lett.* **2003**, *3*, 1569–1572.
- (20) Sun, Y. G.; Mayers, B. T.; Xia, Y. *Nano Lett.* **2002**, *2*, 481–485.
- (21) Lu, X. M.; Tuan, H. Y.; Chen, J. Y.; Li, Z. Y.; Korgel, B. A.; Xia, Y. *J. Am. Chem. Soc.* **2007**, *129*, 1733–1742.
- (22) Luther, J. M.; Zheng, H. M.; Sadtler, B.; Alivisatos, A. P. *J. Am. Chem. Soc.* **2009**, *131*, 16851–16857.
- (23) Son, D. H.; Hughes, S. M.; Yin, Y. D.; Alivisatos, A. P. *Science* **2004**, *306*, 1009–1012.
- (24) Wark, S. E.; Hsia, C. H.; Son, D. H. *J. Am. Chem. Soc.* **2008**, *130*, 9550–9555.
- (25) Grzybowski, B. A. *Chemistry in Motion: Reaction-Diffusion Systems for Micro- and Nanotechnology*; Wiley: Chichester, U.K., 2009.
- (26) Schadt, M. J.; Cheung, W.; Luo, J.; Zhong, C. *J. Chem. Mater.* **2006**, *18*, 5147–5149.
- (27) Maye, M. M.; Zhong, C. *J. Mater. Chem.* **2000**, *10*, 1895–1901.
- (28) Kariuki, N. N.; Luo, J.; Maye, M. M.; Hassan, S. A.; Menard, T.; Naslund, H. R.; Lin, Y. H.; Wang, C. M.; Engelhard, M. H.; Zhong, C. *J. Langmuir* **2004**, *20*, 11240–11246.
- (29) Dick, K.; Dhanasekaran, T.; Zhang, Z. Y.; Meisel, D. *J. Am. Chem. Soc.* **2002**, *124*, 2312–2317.
- (30) Ashby, M.; Shercliff, H.; Cebon, D. *Materials Engineering Science Processing and Design*, 1st ed.; Elsevier: New York, 2007.
- (31) Ouyang, G.; Tan, X.; Wang, C. X.; Yang, G. W. *Chem. Phys. Lett.* **2006**, *420*, 65–70.
- (32) Fan, H. J.; Gosele, U.; Zacharias, M. *Small* **2007**, *3*, 1660–1671.
- (33) Ferrando, R.; Jellinek, J.; Johnston, R. L. *Chem. Rev.* **2008**, *108*, 845–910.
- (34) Link, S.; Wang, Z. L.; El-Sayed, M. A. *J. Phys. Chem. B* **1999**, *103*, 3529–3533.
- (35) Lee, K. S.; El-Sayed, M. A. *J. Phys. Chem. B* **2005**, *109*, 20331–20338.
- (36) Link, S.; Burda, C.; Wang, Z. L.; El-Sayed, M. A. *J. Chem. Phys.* **1999**, *111*, 1255–1264.
- (37) Moores, A.; Goettmann, F. *New J. Chem.* **2006**, *30*, 1121–1132.
- (38) Shibata, T.; Bunker, B. A.; Zhang, Z. Y.; Meisel, D.; Vardeman, C. F.; Gezelter, J. D. *J. Am. Chem. Soc.* **2002**, *124*, 11989–11996.
- (39) (a) Hodak, J. H.; Henglein, A.; Giersig, M.; Hartland, G. V. *J. Phys. Chem. B* **2000**, *104*, 11708–11718. (b) Hu, M.; Hartland, G. V. *J. Phys. Chem. B* **2002**, *106*, 7029–7033. (c) Wang, X.; Zhang, Z.; Hartland, G. V. *J. Phys. Chem. B* **2005**, *109*, 20324–20330. (d) Hu, M.; Petrova, H.; Hartland, G. V. *Chem. Phys. Lett.* **2004**, *391*, 220–225. (e) Hu, M.; Petrova, H.; Sekkinen, A. R.; Chen, J.; McLellan, J. M.; Li, Z.-Y.; Marquez, M.; Li, X.; Xia, Y.; Hartland, G. V. *J. Phys. Chem. B* **2006**, *110*, 19923–19928.
- (40) Zhang, Q. B.; Lee, J. Y.; Yang, J.; Boothroyd, C.; Zhang, J. X. *Nanotechnology* **2007**, *18*, 245605.
- (41) Freeman, R. G.; Hommer, M. B.; Grabar, K. C.; Jackson, M. A.; Natan, M. J. *J. Phys. Chem.* **1996**, *100*, 718–724.
- (42) Mulvaney, P. *Langmuir* **1996**, *12*, 788–800.
- (43) (a) Gerbec, J. A.; Magana, D.; Washington, A.; Strouse, G. F. *J. Am. Chem. Soc.* **2005**, *127*, 15791–15800. (b) Washington, A. L.; Strouse, G. F. *J. Am. Chem. Soc.* **2008**, *130*, 8916–8922.
- (44) Han, H.; Di Francesco, G.; Maye, M. M. *J. Phys. Chem. C* **2010**, *114*, 19270–19277.
- (45) (a) Draine, B. T.; Flatau, P. J. *J. Opt. Soc. Am. A* **1994**, *11*, 1491–1499. (b) Draine, B. T.; Flatau, P. J. *User Guide to the Discrete Dipole Approximation Code DDSCAT 7.0*; 2008; <http://arXiv.org/abs/0809.0337v5>. (c) Draine, B. T.; Flatau, P. J. *J. Opt. Soc. Am. A* **2008**, *25*, 2693–2703.
- (46) (a) Sherry, L. J.; Jin, R. C.; Mirkin, C. A.; Schatz, G. C.; Van Duyne, R. P. *Nano Lett.* **2006**, *6*, 2060–2065. (b) Kelly, K. L.; Coronado, E.; Zhao, L. L.; Schatz, G. C. *J. Phys. Chem. B* **2003**, *107*, 668–677.
- (47) Mallin, M. P.; Murphy, C. J. *Nano Lett.* **2002**, *2*, 1235–1237.
- (48) Chen, J. Y.; Wiley, B.; McLellan, J.; Xiong, Y. J.; Li, Z. Y.; Xia, Y. *Nano Lett.* **2005**, *5*, 2058–2062.
- (49) Moskovits, M.; Srnova-Sloufova, I.; Vlckova, B. *J. Chem. Phys.* **2002**, *116*, 10435–10446.
- (50) Bok, H. M.; Shuford, K. L.; Kim, S.; KyuKim, S.; Park, S. *Langmuir* **2009**, *25*, 5266–5270.
- (51) Denbigh, K. *The Principles of Chemical Equilibrium*, 4th ed.; University Press: Cambridge, U.K., 1981.
- (52) Gersten, J. I.; Smith, F. W. *The Physics and Chemistry of Materials*; John Wiley & Sons: New York, 2001.
- (53) Alloyeau, D.; Ricolleau, C.; Motte, C.; Oikawa, T.; Langlois, C.; Le Bouar, Y.; Braidy, N.; Loiseau, A. *Nat. Mater.* **2009**, *8*, 940–946.
- (54) Qi, W.; Li, Y.; Xiong, S.; Lee, S. T. *Small* **2010**, *6*, 1996–1999.
- (55) Takahashi, Y. H.; Ohkubo, T.; Ohnuma, M.; Hono, K. *J. Appl. Phys.* **2003**, *93*, 7166–7168.
- (56) Sato, K.; Hirotsu, Y.; Mori, H.; Wang, Z.; Hirayama, T. *J. Appl. Phys.* **2005**, *98*, 024308.
- (57) Atanasov, I.; Hou, M. *Surf. Sci.* **2009**, *603*, 2639–2651.
- (58) Detor, A. J.; Schuh, C. A. *Acta Mater.* **2007**, *55*, 4221–4232.
- (59) Yang, B.; Asta, M.; Myryasov, O. N.; Klemmer, T. J.; Chantrell, R. W. *Acta Mater.* **2006**, *54*, 4201–4211.
- (60) Kovacs, A.; Sato, K.; Lazarov, V. K.; Galindo, P. L.; Konno, T. J.; Hirotsu, Y. *Phys. Rev. Lett.* **2009**, *103*, 115703.
- (61) Ouyang, G.; Wang, C. X.; Yang, G. W. *Chem. Rev.* **2009**, *109*, 4221–4247.
- (62) Ratke, L.; Voorhees, P. W. *Growth and Coarsening: Ostwald Ripening in Material Processing*; Springer-Verlag: New York, 2002.
- (63) Cho, S.; Jung, S. H.; Lee, K. H. *J. Phys. Chem. C* **2008**, *112*, 12769–12776.
- (64) Tsukahara, Y.; Higashi, A.; Yamauchi, T.; Nakamura, T.; Yasuda, M.; Baba, A.; Wada, Y. *J. Phys. Chem. C* **2010**, *114*, 8965–8970.
- (65) Kappe, C. O. *Angew. Chem., Int. Ed.* **2004**, *43*, 6250–6284.
- (66) Perreux, L.; Loupy, L. *Tetrahedron* **2001**, *57*, 9199–9223.
- (67) Giguere, R. J. *Organic Synthesis: Theory and Application*; JAI Press: Greenwich, CT, 1989.
- (68) Stuerga, D.; Gaillard, P. *Tetrahedron* **1996**, *52*, 5505–5510.
- (69) Von Hippel, A. R. *Dielectric Materials and Applications*; MIT Press: Cambridge, MA, 1954.
- (70) Johnson, P. B.; Christy, R. W. *Phys. Rev. B* **1972**, *6*, 4370–4379.
- (71) Njoki, P. N.; Wu, W.; Zhao, H.; Hutter, L.; Schiff, E. A.; Maye, M. M. *J. Am. Chem. Soc.* **2011**, *133*, 5224–5227.